npj | 2D materials and applications

Article

Published in partnership with FCT NOVA with the support of E-MRS

https://doi.org/10.1038/s41699-025-00587-9

Mobility calculation in disordered WS_2-Al_2O_3 stacks from first principles

Mauro Dossena [1] ✉, Benoit Van Troeye [2], Fabian Ducry [2], Jiang Cao [1], Aryan Afzalian [2], Geoffrey Pourtois [2] & Mathieu Luisier [1] ✉

Transition metal dichalcogenides (TMDCs) are promising candidates for future nano-transistor channels due to their outstanding intrinsic transport properties. However, their electron mobility is highly sensitive to the surrounding dielectric, often falling well below theoretical expectations. In this work, we explore how a stacked Al_2O_3 dielectric affects electron mobility in monolayer WS_2 using first-principles quantum transport simulations. We identify that fluctuations in the electrostatic potential, arising from the disordered structure of Al_2O_3, significantly degrade mobility, especially when WS_2 interfaces with under-coordinated aluminum atoms. Our calculated mobilities ($\simeq$1–30 $cm^2/(V \cdot s)$) align with experimental observations and remain far from the ideal limit ($\simeq$300 $cm^2/(V \cdot s)$). We further demonstrate that encapsulating WS_2 with hexagonal boron nitride (hBN) or employing a crystalline oxide can recover high mobility values. However, these strategies introduce trade-offs in electrostatic control and fabrication complexity, underlining the need for careful dielectric engineering in TMDC-based devices.

The continuous down-scaling of the metal-oxide-semiconductor field-effect transistor (MOSFET) dimensions, together with the integration of evermore active components on the same chip, has been the key enabler of multiple breakthroughs, from personal computers in the 1970's up to smartphones in the 2000' and more recently AI-driven autonomous systems[1]. To keep up with the ever increasing demand for more functionalities and computing power, the semiconductor industry is gradually replacing its current workhorse, the FinFET[2], with gate-all-around transistor architectures based on nano-sheet[3], nano-ribbon[4], or nanowire[5] channels. At the same time, alternatives to strained silicon are actively searched to boost the current of *n*- and *p*-type logic switches[6]. Nano-sheet and nano-ribbon structures lend themselves particularly well to mono- to few-layer two-dimensional (2D) materials, in particular transition metal dicalcogenides (TMDCs)[7,8]. Their carrier mobility is expected to outperform that of Si at similar thicknesses, making them strong contenders as next-generation channel materials[9]. Furthermore, their intrinsic ultra-thin nature provides nearly perfect scaling performance because of their excellent electrostatics. Finally, since they are chemically inert, they tend to form clean interfaces with the surrounding environment, theoretically without dangling bonds.

Despite numerous proof-of-concept demonstrations of 2D MOSFETs in recent years[10–12], several hurdles must still be overcome before unleashing the intrinsic potential of 2D materials. Four major issues are currently plaguing the characteristics of TMDC-based transistors: (i) the in-situ growth of high-quality mono- to few-layer material on suitable substrates[13], (ii) the effective chemical doping of the source and drain extensions[14], (iii) a low-resistance ohmic contacts between metal electrodes and semiconducting channels[15], and (iv) deposition of a high-quality dielectric material on top of the TMDC.

The dielectric environment has been shown to critically affect the electrical properties of TMDC channels, especially when they are interfaced with amorphous (disordered) oxide layers[16]. Due to these oxide layers, the theoretically predicted intrinsic mobility of TMDCs, which is limited by carrier-phonon scattering[17,18], can hardly be reached in experimental settings[19]. The presence of defects within the dielectric layer or of interface roughness between the TMD channel and its surrounding environment typically reduces the performance of 2D MOSFETs: for example by introducing random telegraph noise (RTN), shifting their threshold voltage, degrading their subthreshold slope (SS), or decreasing their ON-state current[20].

To minimize the impact of these dielectric-induced effects on the transport properties of TMDCs, the scientific community is actively looking for insulating materials with high permittivity, low interface trap concentration, flat surface, and large conduction and/or valence band offset with TMDCs, while remaining compatible with today's fabrication processes. On the one hand, standard amorphous oxides grown by Atomic Layer Deposition (ALD) such as SiO_2[21], HfO_2[22], or Al_2O_3[23] have been widely considered, without delivering the expected mobility values. When encapsulated between ALD-grown amorphous oxides, the reported mobility of

[1]Integrated Systems Laboratory (IIS), ETH Zurich, Zurich 8092, Switzerland. [2]Imec, Leuven, 3001, Belgium. ✉e-mail: mdossena@iis.ee.ethz.ch; mluisier@iis.ee.ethz.ch

TMDC never exceeds a few dozen $cm^2/(V \cdot s)$[24]. On the other hand, 2D dielectrics, e.g., hexagonal boron nitride (h-BN)[25] have also received attention as they offer cleaner interfaces than SiO_2, HfO_2, and Al_2O_3. However, the out-of-plane relative permittivity of these 2D dielectrics is relatively low (around 4 for h-BN[26]), which could be problematic in ultra-scaled transistors with gate lengths below 20 nm. Recently, fluorides such as CaF_2 have also been considered due to their interesting dielectric properties (huge bandgap of 12.1 eV and high dielectric constant of 8.43)[27]. However, their use is still limited to proof-of-concept applications because of the difficulty in integrating them into the gate stack.

Atomistic modeling techniques can shed light on the interplay between dielectric layers and 2D materials. Specifically, first-principles methods such as density functional theory (DFT), while still suffering from some drawbacks related to the description of electron-electron correlation, usually offer reliable descriptions of semiconductor-oxide interfaces. Furthermore, they allow to capture the influence of defects or surface roughness on the transport characteristics of TMDCs. Previous studies investigated the structural properties of the interface between TMDCs and crystalline oxides, thus missing important effects associated with the amorphous nature of most oxides[28,29] and of their termination. Indeed, an oxide can show different levels of oxidation/coordination of their metal atoms, especially at the surface, that lead to local interaction of the 2D material with the oxide. We have highlighted the impact of such under- or over-coordination at the surface[30], where hybridization and electrostatic fluctuation appears in the 2D material depending on the oxide termination.

DFT calculations are practical to compute the relaxed geometry, energy levels, and density-of-states of the investigated systems. However, to predict transistors' observables, e.g., carrier mobility or "current vs. voltage" curves, DFT should be combined with a quantum transport solver, giving rise to ab initio device simulations[31]. This powerful approach has been extensively applied to the investigation of 2D MOSFETs, usually under the assumption that the electron/hole wavefunction does not penetrate into the surrounding dielectric layer[32,33]. The latter is therefore omitted from the Hamiltonian matrix describing the structure under test and hard-wall boundary conditions are applied to the surface of the TMDC channel. Defects and/or interface roughness are treated perturbatively, via dedicated scattering rates or self-energies[34]. By doing so, isolating the impact of a defect or interface type becomes rather challenging, as their influence is generally averaged over several configurations and cast into a single representative scattering potential. Any perturbation of the electronic wavefunction because of the environment is also lost with such an approach, while it is captured in a fully-atomistic model of the interface.

In this paper, we address these issues by performing ab initio quantum transport simulations of TMDCs, including their surrounding dielectric layers, based on DFT and the non-equilibrium Green's function (NEGF) formalism[35,36]. The inclusion of the oxide layers in a DFT+NEGF framework allows us to directly assess their influence on the electrical current, without relying on average scattering potentials. The focus is on the technology relevant WS_2-Al_2O_3 system because of its recognized potential as *n*-type MOSFET and its relatively high fabrication maturity[16]. Crucially, the currently available large-scale integration processes limit the deposition of Al_2O_3 to its amorphous phase (am-Al_2O_3) on top of WS_2. Hence, this study concentrates on the effect of amorphous Al_2O_3 on the electron mobility of monolayer WS_2, which is extracted with the help of the well-known "dR/dL" (or transmission line) method[37,38]. As expected, we find that the mobility depends on the interface quality and on the defect density. Based on these results, we propose theoretical solutions to enhance the mobility of WS_2-Al_2O_3 MOSFETS and discuss the challenges to be overcome for practical realization.

Results and Discussion

All mobility calculations start by constructing super-cells comprising a WS_2 monolayer and defective am-Al_2O_3 following the precepts of ref. 30. There is indeed little information available experimentally on the morphology of the interface between WS_2 and am-Al_2O_3, and we thus have to consider different possibilities for the termination of the oxide. Given that am-Al_2O_3 is typically deposited via water-based ALD and followed by hydrogen annealing, we adopted the reasonable assumption that the interface is hydrogen-terminated. The main structural degree of freedom remaining is the coordination of the Al atoms at the interface, which has not yet been experimentally resolved. To explore the impact of this parameter, we constructed several interface models by varying the Al coordination and analyzing the resulting structures (see ref. 30 for more details). We consider here 3 interface configurations, as depicted in Fig. 1. They correspond to possible coordinations of the Al and O atoms at the interface with a monolayer WS_2: undercoordinated Al atoms (*sharpcut-x4*), correctly-coordinated (*roughcut*) and overcoordiates Al atoms (*sharpcut-x6*). In all cases, a pristine WS_2 super-cell of dimensions $3.1 \times 1.6\ nm^2$ in the *x*-*z* plane is first relaxed with the CP2K DFT package[28] before amorphous Al_2O_3 layers with different surfaces but fixed thickness of around t_y=1.0 nm are stacked on top of it. Hydrogen atoms are added at the interface to passivate the remaining oxygen dangling bonds. The whole stack is subsequently relaxed. During this process, the W atomic layer is kept fixed to avoid strong monolayer bending caused by the relatively small dimensions of the chosen super-cell. All other degrees of freedom (atomic positions and out-of-plane lattice component) are optimized. Note that periodic boundary conditions are applied along the *y* axis so that the same Al_2O_3 layers is present on both sides of WS_2. More details about the structural relaxation and the generation of amorphous oxide layers can be found in the Method section and in ref. 30.

Each of the three selected interfaces exhibits peculiar features that are correlated to the procedure used to create them. In the first configuration labeled *sharpcut-x4* (Fig. 1a), the WS_2-am-Al_2O_3 interface is oxygen-poor so that several Al atoms are left under-coordinated and tend to form covalent bond with WS_2. They are not passivated with H atoms. Since there are two

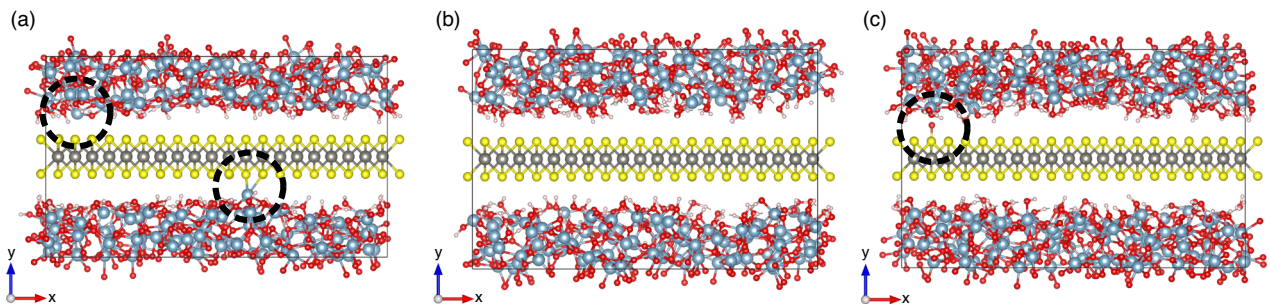

Fig. 1 | Atomistic structure of the three investigated am-Al_2O_3-WS_2 interfaces. Every colored sphere represents a different atomic species: red, O; light blue, Al; white, H; yellow, S; grey, W. The figures were rendered with the VESTA software[61]. **a** *Sharpcut-x4* configuration: the am-Al_2O_3-WS_2 interface is oxygen-poor so that several Al atoms are left under-coordinated. As a consequence, the highlighted Al atoms bond with WS_2. **b** *Roughcut* configuration: all interface atoms reproduce the bulk coordination. **c** *Sharpcut-x6* configuration: the am-Al_2O_3-WS_2 interface is over-saturated with oxygen atoms, leaving some Al atoms over-coordinated. Hence, the marked surface O atom is adsorbed by the WS_2 layer.

under-coordinated Al atoms per super-cell, the defect density can be estimated to be 4e13 cm^{-2}. In the second configuration named *roughcut* (Fig. 1b), all Al and O atoms at the interface with WS_2 have the right coordination. No bond is formed between the oxide and the semiconductor layers, thus maintaining a *quasi* van der Waals gap between them. Finally, in the third configuration, *sharpcut-x6* (Fig. 1c), the am-Al_2O_3-WS_2 interface is over-saturated with oxygen atoms, which leads to the adsorption of oxygen atoms within the WS_2 monolayer. In this case, one oxygen atom is adsorbed, corresponding to a defect density of 2e13 cm^{-2}. It should be emphasized that all *sharpcut* structures are obtained by cutting away atoms from the surface of bulk am-Al_2O_3 with a flat plane, while the *roughcut* geometry keeps some atoms out of the slab upon construction in order to preserve the surface Al coordination the closest as possible to its value in the bulk oxide. The remaining oxygen dangling bonds are passivated with hydrogen atoms in all cases.

The produced *sharpcut* and *roughcut* super-cells serve as basis to generate full device structures from which mobility values can be computed. These devices consist of a central part, which is made of the repetition of WS_2-am-Al_2O_3 cells, plus side extensions composed of pristine WS_2. The Hamiltonian (H) and overlap (S) matrices of the full samples are assembled from DFT calculations of the individual elements with the CP2K package[28]. These matrices are then passed to an in-house DFT+NEGF solver called OMEN that takes them as inputs to calculate the electrical current flowing through the corresponding devices and the associated electron density[39]. By varying the number of repeated WS_2-am-Al_2O_3 super-cells, the device length along the x axis (L) can be modified and its resistance can be evaluated as a function of this parameter. Following the "dR/dL" method[37,38], the electron mobility is finally computed. This approach is summarized in Fig. 2 where the final device structure is schematized as well. More details about the DFT+NEGF approach can be found in the Method section.

The mobility of WS_2 transistors is limited not only by the presence of insulator layers around the channel, but also by electron-phonon (e-ph) interactions. In general, the latter cannot be eliminated and should therefore be taken into account. Moreover, e-ph scattering breaks phase coherence and helps avoid nonphysical resonance effects arising in disordered structures[37]. If electron-phonon scattering is omitted and a fully coherent transport calculation is performed, quantum interferences dominate and obscure the diffusive transport regime, making the application of the dR/dL method unreliable (see Fig. S1 in the Supplementary Material). To minimize computational burden, we employ a phenomenological e-ph model based on the deformation potential theory of the WS_2 monolayer (see Method section). The strength of the electron-phonon coupling, which takes the form of a single parameter, is adjusted to reproduce the electron mobility of pristine WS_2 that we previously calculated from first-principles with the linearized Boltzmann transport equation (335 $cm^2/(V \cdot s)$ at low electron concentration)[17]. Under similar conditions, our phenomenological model returns a phonon-limited mobility of 312 $cm^2/(V \cdot s)$ for pristine WS_2. The atomic structure that was used for this calculation, its electronic bandstructure, and the application of the dR/dL method are displayed in Fig. 3. In principle, each structure would require its own deformation potential, as the dielectric environment has been shown to significantly affect electron-phonon scattering in 2D materials, both by screening the intrinsic phonon modes of WS_2 and by introducing additional remote phonon scattering mechanisms[40]. This goes, however, beyond the scope of this paper, which focuses on the role played by the oxide layer disorder. Also, including the true e-ph scattering coupling from ab initio calculation would be computationally too intensive for the disordered structures investigated here. In other words, we capture here the impact of the dielectric on the electronic properties of the 2D materials, not on its vibration.

Next, to determine the influence of the am-Al_2O_3 dielectric on the transport properties of WS_2, we examine in Fig. 4a the lowest conduction bands of the *sharpcut-x4* super-cell shown in Fig. 1. All bands have a distinct WS_2 character, as can be inferred from the projected density-of-states plotted in Fig. S2 in the Supplementary Material (SM), i.e., the electronic states are confined within the WS_2 monolayer. Notably, an almost flat band (not shown here) is present below the conduction band edge, at an energy of around 8.5 eV. It reveals the existence of a localized state originating from the strong hybridization between the exposed Al atom in the bottom layer and the WS_2 just above (Fig. 1a). We neglect this band in our transport calculations as it does not host mobile charges and as such does not contribute to the current.

A key feature of the interface bandstructure in Fig. 4a is that all bands are much flatter than in the pristine WS_2 case, with a reduction of the electron velocity and thus mobility as direct consequences. Flat bands are usually associated with structural disorder[41], which is not intrinsically present in the WS_2 monolayer, but induced by the adjacent am-Al_2O_3 layer.

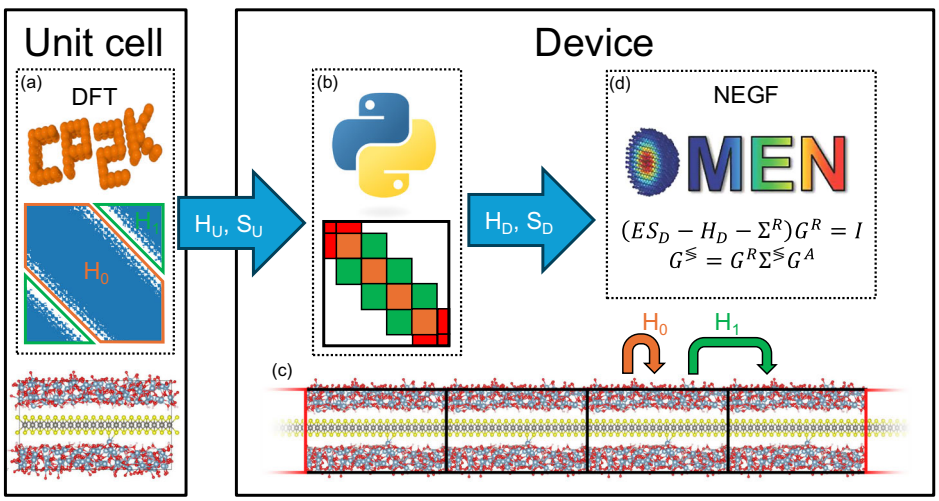

Fig. 2 | Summary of the method developed to simulate electron transport through WS_2-Al_2O_3 stacks. a After constructing a unit cell containing both materials[30], its Hamiltonian H_U and overlap S_U matrices are calculated with the CP2K package[28] (left). The unit cell Hamiltonian H_U is decomposed into its in-cell coupling matrix H_0 (highlighted in orange) and its coupling to the next cell, H_1 (green). Similar blocks can be extracted from S_U. **b** All these blocks are repeated to create the Hamiltonian H_D and overlap S_D matrices of the device of interest. The latter is composed of N repetitions of the same super cell, with N between 3 and 5. Pristine monolayer WS_2 cells are then added on both sides of the generated structure to form semi-infinite contacts and enable the scattering-free injection of electrons into the resulting open system. Python scripts are used for that purpose. The final Hamiltonian H_D is shown in the middle. **c** The atomic lattice of the full device is depicted at the bottom. The unit cell Hamiltonian blocks H_0 and H_1 are indicated by arrows and colors. (d) Once H_D and S_D are available, the quantum transport properties of the constructed device can be computed with the OMEN solver[39]. The detailed procedure is explained in the Method section.

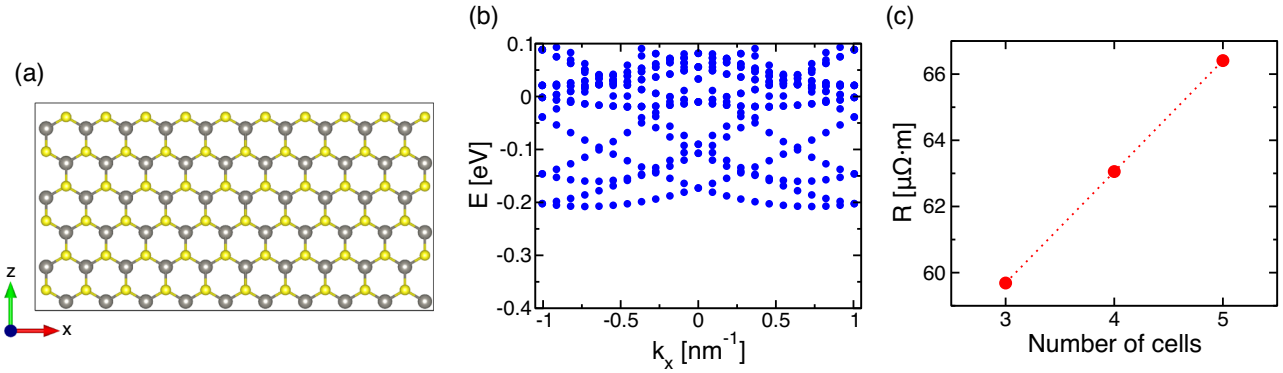

Fig. 3 | Illustration of the dR/dL method for the electron mobility of pristine WS_2. **a** Top view of the $10 \times 3\sqrt{3}$ WS_2 supercell employed for that purpose. Grey spheres represent W atoms, while yellow ones refer to S atoms. **b** Corresponding electronic bandstrucure of pristine WS_2 along the *x*-axis in sub-plot (**a**) from *Γ* high-symmetry. **c** Electrical resistance of the sample in sub-plot (**a**) at an electron concentration n=1.9e13 cm^{-2} as a function of its length along the *x*-axis. The latter is given in unit cells, each of them measuring 3.13 nm in length along *x*. The red dots are the calculated resistance values, the dotted line is a linear fit to this data.

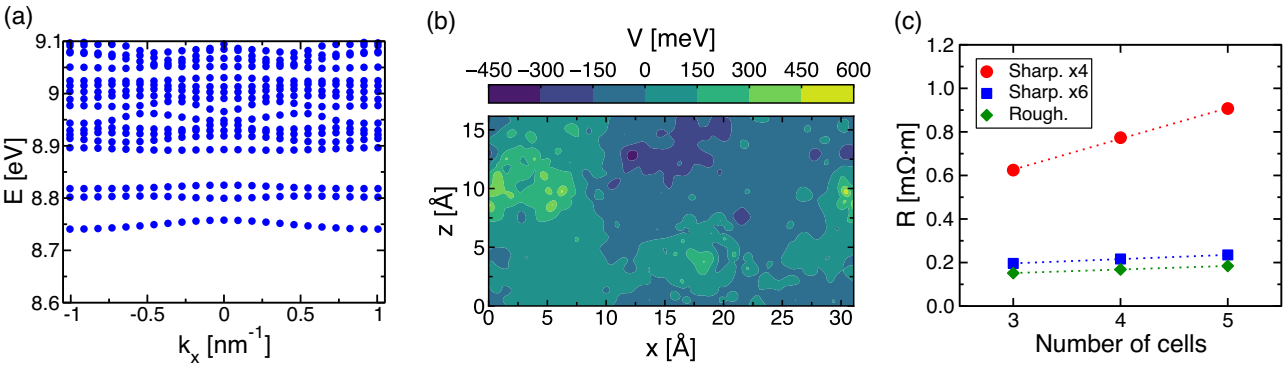

Fig. 4 | Electron mobility calculation of the different am-Al_2O_3-WS_2 interface models investigated using the dR/dL method. **a** Lowest conduction bands of the *sharpcut-x4* super-cell from Fig. 1 along the transport direction *x* from the zone-center. **b** Spatially-resolved electrostatic potential extracted in the *x*-*z* plane formed by the W atoms for the same *sharpcut-x4* super-cell as in (**a**). **c** Electrical resistance as a function of the device length (given in terms of repeated super-cell) for the three considered interfaces: *sharpcut-x4* (red circles, n=1.6e13 cm^{-2}), *roughcut* (green diamonds, n=1.7e13 cm^{-2}), and *sharpcut-x6* (blue squares, n=1.8e13 cm^{-2}). The dotted lines represent linear fits.

Table 1 | Mobility values μ, electron concentration n, and linearity factor α for the different WS_2-am-Al_2O_3 interface configurations investigated in this work

	n (cm^{-2})	μ ($cm^2/(V \cdot s)$)	α
WS_2	1.9e13	312.0	0.99998
Sharpcut-x4	1.6e13	8.5	0.99067
Roughcut	1.7e13	69.7	0.99996
Sharpcut-x6	1.8e13	56.5	0.99351

The results for pristine WS_2 are also shown for sake of reference. They include electron-phonon scattering only, through the aforementioned phenomenological model.

Hence, the origin of the flat dispersion in the *sharpcut-x4* super-cell can be traced back to local variations of the electrostatic potential. Fig. 4b reports the difference in electrostatic potential between the pristine WS_2 and *sharpcut-x4* am-Al_2O_3-WS_2 configurations in the form of a color map. A strong modulation of the electrostatic potential can be observed. It comes from the presence of the amorphous oxide, which creates potential barriers and wells. Possible explanations for these variations are suggested in ref. 42, e.g., the presence of charged oxide defects or hybridization between the oxide and monolayer electronic states. From the electrostatic potential modulation, we can estimate the barrier height ΔV that electrons feel by taking the energy difference between the minimum and the maximum value of this quantity, neglecting sharp peaks and wells. For *sharpcut-x4*, we find that $\Delta V \approx 0.75$ eV.

By repeating the *sharpcut-x4* super-cell 3, 4, and 5 times along the transport direction (*x*), devices of different lengths L can be constructed and their resistance $R(L)$ computed as a function of L. To be able to apply the dR/dL method, $R(L)$ should increase linearly with L. A linear increase of $R(L)$ usually indicates "diffusive transport". This critical property is ensured in our am-Al_2O_3-WS_2 systems, as demonstrated in Fig. 4c. It can be quantified by defining a linearity factor α according to ref. 43 (more detail in the Method section). Ideally, α should be equal to 1 to ensure a linear dependence of R on L. This is generally achieved by considering several samples per interface configuration (*sharpcut-x4*, *roughcut*, and *sharpcut-x6*), each of them with a different realization of the amorphous oxide. In doing so, the final $R(L)$ is computed by taking the average of all structures corresponding to the length L. However, by repeating the same defective super-cell along *x*, as here, it was shown in ref. 37 that the number of samples can be greatly reduced. We found that a single structure is sufficient to obtain a linear dependence of the resistance on the length and a reasonable estimate of the mobility. The key factor is the inclusion of electron-phonon scattering as it reduces the effect of coherent interference patterns, which are particularly strong when repeating the same defective super-cell.

All calculated mobility values μ and linearity factors α are summarized in Table 1 at similar electron concentrations (between 1.6 and 1.8e13 cm^{-2}). The lowest μ (8.5 $cm^2/(V \cdot s)$) is obtained for the *sharpcut-x4* structure, with a 35 × reduction as compared to pristine WS_2. The large electrostatic potential variations observed in this case significantly deteriorate the transport properties of WS_2. They come from the presence of under-coordinated Al atoms and constantly modify the electron trajectories. The *roughcut* interface leads to a much higher mobility of 69.7 $cm^2/(V \cdot s)$. Since no bonding occurs between the am-Al_2O_3 and WS_2 layers in this configuration (Fig. 1b), the interface quality is substantially better. Nonetheless, large potential modulations can still be identified (Fig. S3 in the SM), but their amplitude ($\Delta V \approx 0.4$ eV) is smaller than in the *sharpcut-x4* geometry, thus explaining the 8 × higher mobility. The last structure (*sharpcut-x6*) shows a mobility value close to the *roughcut* case (μ=56.5 $cm^2/(V \cdot s)$) with which it shares a similar electrostatic potential modulation profile ($\Delta V \approx$ 0.4 eV), except that very localized wells are present, caused by the adsorbed oxygen atoms (Fig. S4 in SM). Because of their well-shape, they have little impact on electron transport, but would negatively affect hole transport.

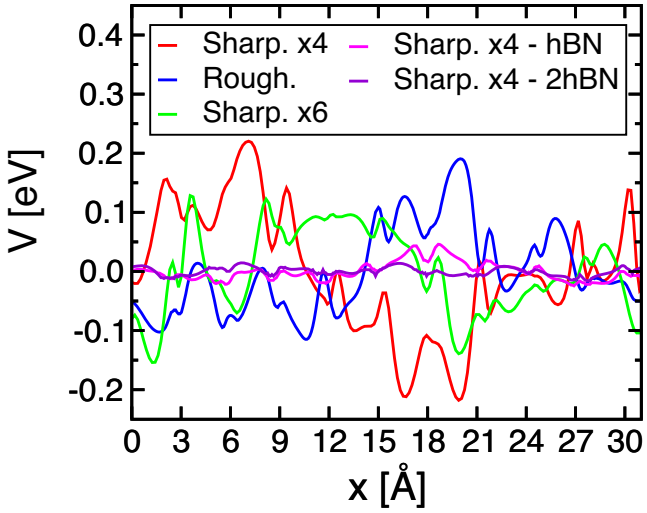

Fig. 5 | Electrostatic potential fluctuations extracted along a line through the center of the WS_2 channel for all structures incorporating amorphous Al_2O_3. The red curve corresponds to *sharpcut-x4*, the blue to *roughcut*, the green to *sharpcut-x6*, the magenta to *sharpcut-x4* with one hBN layer, and the purple to *sharpcut-x4* with two hBN layers.

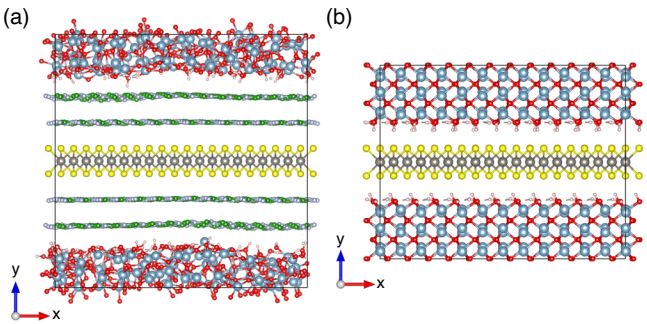

Fig. 6 | Atomistic structure of modified WS_2-Al_2O_3 interfaces. Every colored sphere represents a different atomic species: red, O; light blue, Al; white, H; yellow, S; gray, W; green, B; light violet, N. **a** *Sharpcut-x4* structure where WS_2 is encapsulated between 2 hBN layers before Al_2O_3 is added. **b** Sapphire Al_2O_3-WS_2 structure.

Reported experimental mobility values for monolayer WS_2-am-Al_2O_3 transistors range between 1 and 30 $cm^2/(V \cdot s)$[24,44]. Our calculations return higher values for the cleaner samples *roughcut* and *sharpcut-x6*, but the *sharpcut-x4* results are in line with experiments. It is nevertheless expected that calculated mobilities exceed measured ones because our model does not consider all possible scattering sourced in 2D TMDC-based transistors. Defects localized in WS_2[45] and interactions with dielectric optical phonons through long-range electrostatics[40,46] are omitted. While the impact of localized defects in WS_2, such as grain boundaries and vacancies, is expected to be minor in high-quality samples with mobilities exceeding 100 $cm^2/(V \cdot s)$[13], the contribution of remote phonon scattering can be more significant. In particular, for SiO_2-WS_2-ZrO_2 heterostructures, interactions with remote phonons have been shown to reduce the mobility down to ~35 $cm^2/(V \cdot s)$[40], a value comparable to those reported in this work. This suggests that including remote phonon scattering would further decrease the mobilities we calculated. Still, it appears that under-coordinated Al atoms could be the principal mechanism behind the generally low mobility of WS_2-am-Al_2O_3 stacks.

It is important to note that, due to computational limitations, this study includes only a single realization of each interface type. To verify the consistency of our results, we computed the mobility for one additional

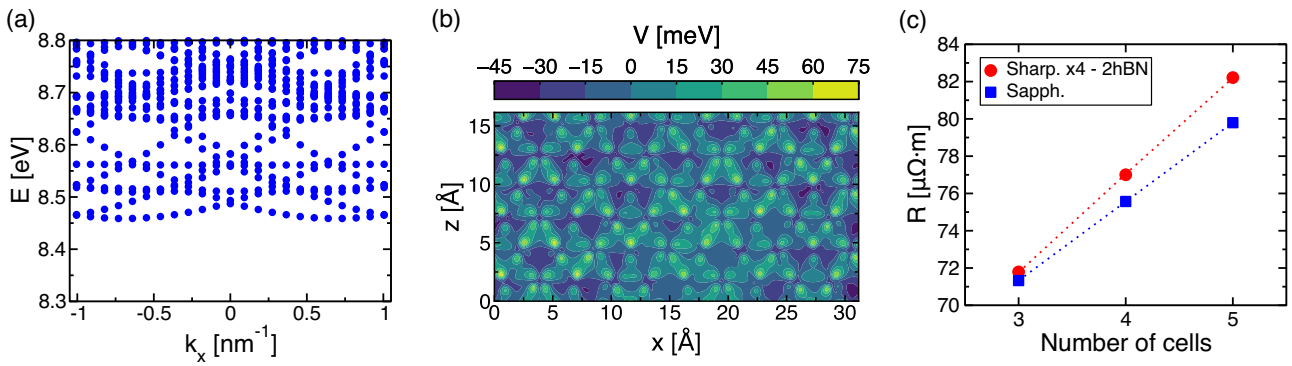

Fig. 7 | Electron mobility calculation of WS_2-Al_2O_3 structures with extra encapsulation hBN layers (2 on each side) and H-terminated sapphire. **a** Conduction band of the am-Al_2O_3-hBN-WS_2-hBN-am-Al_2O_3 stack with the *sharpcut-x4* oxide as a function of k_x from the zone-center. **b** Spatially-resolved electrostatic potential modulation extracted in the *x*-*z* plane formed by the W atoms of the structure in (**a**). **c** Electrical resistance as a function of the device length for the sapphire - WS_2 - sapphire (blue squares) and am-Al_2O_3-hBN-WS_2-hBN-am-Al_2O_3 (red circles) structures from Fig. 6. The dotted lines are linear fits of the data.

Table 2 | Mobility values μ, electron concentration n, and linearity factor α for the modified WS_2-Al_2O_3 structures

	n (cm^{-2})	μ ($cm^2/(V \cdot s)$)	α
Sharpcut-x4-2hBN	1.7e13	247	0.99951
Sharpcut-x4-hBN	1.7e13	131.3	0.97534
Sapphire	1.5e13	219.1	0.99999
Sapphire-4 Def.	1.9e13	211.7	0.99936
Sapphire-8 Def.	1.9e13	161.6	0.99512

roughcut sample generated from a different amorphous seed. The resulting mobility, available in the Fig. S5 in the SM, closely matches the previously reported value for the *roughcut* case (54.3 vs. 69.7 $cm^2/(V \cdot s)$). Nonetheless, drawing statistically meaningful conclusions would require generating and analyzing multiple interface configurations. Such an investigation is beyond the scope of the present work, which aims to identify general trends based on the available set of samples, in particular the important role of electrostatic potential modulations and of surrounding hBN layers.

Next, we propose two approaches to restore the mobility of a WS_2 monolayer embedded within a dielectric environment. Given the correlation between electrostatic potential modulations and mobility degradation, possible solutions consist of engineering the semiconductor-oxide interfaces to minimize the influence of potential variations on carrier transport. First, we can move away the am-Al_2O_3 layer from the channel by encapsulating WS_2 between 2D dielectric layers with clean surfaces, e.g., hexagonal boron nitride, as suggested in[47] and depicted in Fig. 6(a).

To test this method, we consider the am-Al_2O_3 layer with the lowest mobility, *sharpcut-x4*. This oxide is no longer in direct contact with WS_2, but separated by an hBN bilayer, thus reducing their interactions. Indeed, hBN has been widely used as a dielectric for devices based on 2D materials, because of its ability to form van der Waals interfaces with TMDCs. Furthermore, it has been observed that hBN improves the electron mobility of encapsulated 2D materials[25]. To construct our stack in Fig. 6a, hBN is strained by 1.8% to match the in-plane lattice constant of WS_2. Then the same relaxation procedure as for *sharpcut-x4* is applied, that is, keeping the in-plane lattice vectors and the W atom positions fixed while relaxing all remaining degrees of freedom. It can be seen that the hBN layer closer to am-Al_2O_3 shows corrugation, whereas the one closer to WS_2 remains almost perfectly flat.

Alternatively, as a second approach, the homogeneity of the dielectric could be improved by employing a crystalline oxide instead of an amorphous one. In Fig. 6b we show a structure where am-Al_2O_3 is replaced by crystalline α-Al_2O_3 (sapphire) with an OH-terminated surface in contact with WS_2. To generate this structure, the sapphire cell was strained by 1.9% to match the dimensions of a 2.8×1.6 nm^2 WS_2 layer. While promising, the applicability of this solution is currently hindered by manufacturing limitations. Scalable growth of crystalline Al_2O_3 on top of WS_2 is not yet possible. Transfer methods were proposed, but they are still at an early stage of development[48].

Figure 7a reports the bandstructure along the transport direction for the *sharpcut-x4* structure with an hBN bilayer surrounding the WS_2 channel on each side. The band dispersion is no longer as flat as in Fig. 4a where the am-Al_2O_3 oxide is in direct contact with the semiconductor, and much closer to the results of pristine WS_2 (Fig. 3a). This clearly indicates that the extra hBN encapsulation decreases the influence of the oxide. Still, few defect levels appear in the bandstructure, at energies close to 8.7 eV. They have a flatter dispersion and correspond to states located within the oxide, not in WS_2.

The reduced impact of the oxide is confirmed by the electrostatic potential modulation in Fig. 7b. The variations are much smaller ($\Delta V \approx$ 45 meV) than without the hBN bilayers and exhibit a quasi-periodic pattern, similar to the structure of WS_2. Figure 7c displays the "resistance vs. sample length" of the stack with hBN bilayers (labeled *sharpcut-x4-2hBN* in Table 2) from which a mobility μ=247 $cm^2/(V \cdot s)$ can be extracted at an electron concentration n=1.7e13 cm^{-2}. This result demonstrates the usefulness of introducing hBN bilayers. The slight mobility reduction with respect to the pristine case can be attributed to the residual electrostatic potential modulations.

Next, we remove one of the hBN layers on each side of the WS_2 channel. In this case labeled *sharpcut-x4-hBN* in Table 2, the calculated mobility decreases to 131.3 $cm^2/(V \cdot s)$ at the same electron concentration as before (n=1.7e13 cm^{-2}). With a shorter distance between am-Al_2O_3 and WS_2, defects at the oxide surface modulate the electrostatic potential of the channel more strongly (Fig. S6 in SM), leading to a barrier $\Delta V \approx$ 160 meV and to a deterioration of the transport properties. The mobility is still more than one order of magnitude larger than without any hBN layer (8.5 $cm^2/(V \cdot s)$ at n=1.6e13 cm^{-2}, see Table 1).

It should, however, be emphasized that the encapsulation of WS_2 with hBN comes at the expense of either reduced electrostatic control or increased gate leakage. Using a simplified series capacitance model, we relate the combined thickness of the hBN and Al_2O_3 gate oxides to the widely used Equivalent Oxide Thickness (EOT) metric (see Methods for details). Reaching an equivalent oxide thickness (EOT) of 0.9 nm, as prescribed by the International Roadmap for Devices and Systems for the year 2028[49], requires an am-Al_2O_3 thickness of 2.1 nm. If one (two) hBN layers are inserted between the WS_2 channel and the oxide, the am-Al_2O_3 thickness cannot exceed 1.2 (0.4) nm to obtain the same EOT as before because of the lower permittivity of hBN (ϵ_R=3.3 along the out-of-plane direction[26]) compared to Al_2O_3 (ϵ_R=9). With an effective "hBN plus am-Al_2O_3" thickness of 1.5 (1.0) nm, gate leakage currents cannot be suppressed from the *sharpcut-x4-hBN* (*sharpcut-x4-2hBN*) structure.

If am-Al_2O_3 is replaced by crystalline α-Al_2O_3, the resulting stack labeled *sapphire* in Table 2 provides a high mobility μ=219.1 $cm^2/(V \cdot s)$ at n=1.5e13 cm^{-2}. In this configuration, the electrostatic potential modulations, shown in Fig. S7 in SM, are fully periodic. The potential barriers do not completely vanish ($\Delta V \approx$ 160 meV), but they are smaller than in all amorphous cases. Their presence can be attributed to the lattice mismatch between α-Al_2O_3 and WS_2, which leads to a repeating atomic pattern at the interface. Consequently, this pattern induces a periodic potential experienced by electrons within WS_2. This effect is at the origin of the mobility decrease, compared to the pristine case. Since defect-free interfaces probably do not exist, we also tried to remove hydrogen passivation atoms from the sapphire surface, exposing the WS_2 channel to uncharged oxygen dangling bonds. With 4 (8) dangling bonds per super-cell corresponding to a defect concentration of 8.75e13 cm^{-2} (1.75e14 cm^{-2}), the mobility of the *sapphire-4 Def.* (*sapphire-8 Def.*) structure decreases to 211.7 $cm^2/(V \cdot s)$ (161.6 $cm^2/(V \cdot s)$) at n =1.9e13 cm^{-2}. Despite these very high defect concentrations and the fact that they generate non-negligible potential barriers (Figs. S8 and S9 in SM), the mobility remains relatively high. The situation is different, if the dangling bonds are charged[50]. Hence, even with crystalline oxides, the interface with semiconductors may play a crucial role. A comprehensive overview of the resistance, electron concentration, mobility, and linearity factor across all structures is provided in Fig. S10 in the SM.

In this work, we developed a framework to simulate electron transport through Al_2O_3-WS_2 stacks and extract their mobility. By directly including the amorphous oxide into our ab initio quantum transport domain, the WS_2-am-Al_2O_3 interface can be accurately described, without relying on external fitting parameters or simplified models. Calculations under different interface configurations revealed that oxide-induced electrostatic potential modulations in the WS_2 channel are responsible for mobility degradation, up to 35× compared to the pristine case. Similar mobility degradations are reported in experimental settings. In particular, under-coordinated aluminum atoms at the semiconductor-oxide interface lead to the strongest

potential modulations, whereas the impact of extra oxygen atoms in this region is less important. Even in the optimistic scenario of perfectly coordinated am-Al_2O_3 surfaces, residual potential variations still affect the electron mobility, nevertheless to a smaller extent. Finally, we demonstrated that encapsulating the WS_2 channel with hBN layers improves the mobility, but it either reduces the electrostatic control provided by the gate contact or increases gate leakage currents. Sapphire Al_2O_3 was tested as an alternative. It simultaneously preserves high mobility, good electrostatics, and low leakage, but is more difficult to fabricate. Overall, our results allow to extract viable mobility trends and guide the development of 2D MOSFETs. Still, additional simulations will be required to further deepen the understanding of the WS_2 mobility. The inclusion of channel defects, electron-phonon interaction from first principle, surface optical phonons, and more realistic contacts will be needed to improve the model accuracy and predict the mobility of WS_2 and other TMDCs.

Methods

DFT calculation

All DFT calculation are performed with the CP2K package[51], using the GGA-PBEsol exchange-correlation functional[52] with Grimme's DFT-D3(BJ) dispersion correction[53,54]. GTH pseupotentials are employed[55]. For geometry and cell relaxation we use a Triple Zeta Valence Polarized (TZVP) basis set for the W atoms and Double Zeta Valence Polarized (DZVP) for all other atomic species. The structures are relaxed until the forces acting on each atom are smaller than 0.00045 Ha/Bohr and stress is lower than 100 bar. The supercell is restricted to maintaining an orthorhombic structure during relaxation.

The in-plane (*x*-*z*) super-cell size is 31.3 Å × 16.2 Å ($10\times\sqrt{3}$ WS_2 super-cell) for the structure with am-Al_2O_3 and 28.1 Å × 16.2 Å ($9\times\sqrt{3}$ WS_2 super-cell) for sapphire. A shorter super-cell is needed in the sapphire case to obtain a proper lattice matching. A strain lower than 1% is necessary to match the oxides constructed in ref. 30 with our unstrained WS_2 super-cell. The additional oxides required in this work, i.e., sapphire and hBN, were strained by 1.8% and 1.9% respectively. Furthermore, the constructed super-cell is relaxed by fixing the position of the W atoms to avoid any bending of the monolayer and the in-plane lattice vectors to keep WS_2 unstrained. The out-of-plane lattice vector is free to relax so that the separation between the oxide and semiconductor layers automatically adjusts.

To extract the Hamiltonian (H_U) and Overlap (S_U) matrices of the constructed super-cells, a single self-consistent field (SCF) calculation is performed in CP2K with a reduced basis set. A DZVP basis set is chosen for S, W and H, while a Single Zeta Valence (SZV) basis set is selected for Al and O atoms. The usage of a lighter basis set for the oxide allows to reduce the computational intensity of the subsequent quantum transport calculations, without significantly affecting the accuracy of the results around the conduction band edge of the WS_2-am-Al_2O_3 stacks (Fig. S11 in the SM).

Quantum transport

The super-cell Hamiltonian (H_U) and Overlap (S_U) matrices are extracted from the CP2K SCF calculation. The full device matrices are then constructed by repeating the same H_U and S_U several times. The number of repetition defines the length L associated with every device. To inject electrons into the system, two ideal contacts made of the repetition of pristine WS_2 super-cells are added on each side of the device. The coupling elements between these contact and the central, defective region, are equal to the coupling between ideal WS_2 super-cells. By doing this, the Hamiltonian H_D and Overlap S_D matrices of the full device structure are obtained. They are employed to perform NEGF simulations, for which we use the in-house OMEN code[39]. The retarded (G^R), lesser ($G^<$), and greater ($G^>$) Green's functions are computed by solving the following equations:

$$\left(ES_D - H_D - \Sigma^R(E)\right)G^R(E) = I,$$
$$G^{\lessgtr}(E) = G^R(E)\Sigma^{\lessgtr}(E)G^A(E).$$

The self-energies $\Sigma^{R,\lessgtr}$ can be decomposed into a boundary ($\Sigma_B^{R,\lessgtr}$[56]) and a scattering ($\Sigma_S^{R,\lessgtr}$) contribution, the latter obeying the phenomenological electron-phonon scattering model of[32,46]:

$$\Sigma_S^R \approx \frac{\Sigma_S^> - \Sigma_S^<}{2},$$
$$\Sigma_S^{\lessgtr}(E) = D_{ep}^2\Big(\Big(N_{ph}+\tfrac{1}{2}\pm\tfrac{1}{2}\Big)G^{\lessgtr}(E+\hbar\omega) + \Big(N_{ph}+\tfrac{1}{2}\mp\tfrac{1}{2}\Big)G^{\lessgtr}(E-\hbar\omega)\Big),$$

where N_{ph} is the equilibrium Bose-Einstein distribution function, D_{ep} is a deformation potential, and ω is a single phonon frequency. In our room temperature calculations, we set D_{ep}=0.06 eV and $\hbar\omega$=16 meV, which together yield the targeted phonon-limited mobility of monolayer WS_2 (312 $cm^2/(V\cdot s)$ at an electron concentration of 1.9e13 cm^{-2}). Although self-heating effects could, in principle, play a role, under the chosen low-bias conditions (0.001 V), the current does not exceed 10 $\mu A/\mu m$ and therefore remains well below the threshold typically associated with strong self-heating[57,58]. Hence, neglecting self-heating is justified.

To minimize the computational burden and because we rely on large super-cells along the *z*-axis, we sample the Brillouin zone with a single unshifted k-point along the y and z directions. The energy vector E is discretized with an homogeneous interval δE=1 meV. In all quantum transport simulations, a voltage difference δV= 1mV is applied between both extremities of the device structures. The desired electron concentrations are obtained by adjusting the Fermi levels. Poisson's equation is not solved, i.e., we don't add any extra electrostatic term into the DFT Hamiltonian during NEGF calculations. As a consequence, screening effects arising from the excess electron charges are neglected. They are, however, expected to be limited at the electron concentration considered in this study[41].

The current per unit length I and the 2D electron density n are computed from the Green's functions[36]. All aforementioned equations (Green's functions and scattering self-energies) are iteratively solved until current conservation is achieved throughout the entire device. The resistance per unit length R is finally computed as:

$$R = \frac{\delta V}{I}.$$

The atomically resolved electron density n is averaged over the central defective area of the device, neglecting the two super-cells in direct contact with the pristine WS_2 contacts. We observe that the obtained n_{avg} remains constant for all device lengths, as expected. Finally, the mobility is calculated as:

$$\mu = \frac{1}{\frac{dR}{dL}n_{avg}q}, \quad (1)$$

where q is the electron charge and dR/dL is evaluated between two device lengths. Note that the interface between the WS_2 contacts and central WS_2-am-Al_2O_3 region introduces an additional series resistance, besides those originating from the source and drain extensions and from the finite carrier velocity in the contacts (so-called ballistic contact resistance[59]). Since the value of all these components does not depend on the sample length, contrary to the central region covered by an Al_2O_3 layer, their influence vanishes when applying the dR/dL method. This isolates the central device resistance, which can then be directly correlated with the degraded device mobility[37].

An important condition for the dR/dL method validity is the linear dependency of the resistance R with respect to the device length L (diffusive transport). Verifying that this condition is satisfied implies simulating at least three different device lengths. The resistance linearity can then be

determined through the α factor, which is defined as[43]:

$$\alpha = 1 - \frac{\sum_i (R_i - R_i^{fit})^2}{\sum_i (R_i - \overline{R})^2}, \quad (2)$$

where R^{fit} is the linear fitted R at a given length and $\overline{R}$ is the mean resistance over the three different lengths. The closer α is to 1, the more linear the curve is. The minor deviations we observe from the linearity factor, which should ideally be equal to 1, likely stem from numerical sources, such as the discretization of the energy grid or residual errors in the self-consistent solution of the Green's function and scattering self-energy equations.

Electrostatic potential modulation

To compute the electrostatic (Hartree + external) potential modulation induced by the oxide, we subtract to the electrostatic potential in the interface model the potential of the same structure where we have removed the am-Al_2O_3 oxide from the simulation. In this case, the coordinates are not relaxed, but frozen to only capture the change in terms of electronic density. The difference between both electrostatic potentials is then calculated and is referred to as "electrostatic potential modulation". Note that this is a 3D quantity from which we extract the plane corresponding to the position of the W atoms.

Gate thickness estimation

We estimate the full gate capacitance as the series of two single capacitance from the two separate hBN and Al_2O_3 layers. Given the EOT d_{EOT} and the hBN layer thickness d_{hBN}, we compute the total gate thickness (d_{hBN}+d_{Al2O3}) from the series capacitor formula:

$$d_{OX} = \frac{d_{EOT}\varepsilon_{Al_2O_3}}{\varepsilon_{SiO_2}} - d_{hBN}\left(\frac{\varepsilon_{Al_2O_3}}{\varepsilon_{hBN}} - 1\right)$$

where ε_{SiO_2}, ε_{Al2O3}, ε_{hBN} are silicon dioxide, Al_2O_3 and hBN (out of plane) dielectric constants. We choose $\varepsilon_{SiO_2} = 3.9$[60], $\varepsilon_{Al_2O_3} = 9$[60]. d_{hBN} is extracted from our relaxed atomistic supercells, while the thickness dependent ε_{hBN} is taken from literature[26]. In case of one hBN layer, $d_{hBN} = 0.32$ nm, $\varepsilon_{hBN} = 3.29$. If there are two hBN layers, $d_{hBN} = 0.64$ nm, $\varepsilon_{hBN} = 3.44$.

Data availability

Data sets generated during the current study are available from the corresponding author on reasonable request. All DFT input coordinates are provided as Supplementary Material.

Received: 12 March 2025; Accepted: 3 July 2025;
Published online: 01 August 2025

References

1. Cavin, R. K., Lugli, P. & Zhirnov, V. V. Science and engineering beyond Moore's law. *Proc. IEEE* **100**, 1720–1749 (2012).
2. Xie, R. et al. A 7nm finfet technology featuring euv patterning and dual strained high mobility channels. In *2016 IEEE international electron devices meeting (IEDM)*, 2–7 (IEEE, 2016).
3. Jagannathan, H. et al. Vertical-transport nanosheet technology for CMOS scaling beyond lateral-transport devices. In *2021 IEEE International Electron Devices Meeting (IEDM)*, 26–1 (IEEE, 2021).
4. Radosavljević, M. et al. Demonstration of a stacked CMOS inverter at 60nm gate pitch with power via and direct backside device contacts. In *2023 International Electron Devices Meeting (IEDM)*, 1–4 (IEEE, 2023).
5. Wu, L. et al. Step-necking growth of silicon nanowire channels for high performance field effect transistors. *Nat. Commun.* **16**, 965 (2025).
6. Cao, W. et al. The future transistors. *Nature* **620**, 501–515 (2023).
7. Fiori, G. et al. Electronics based on two-dimensional materials. *Nat. Nanotechnol.* **9**, 768–779 (2014).
8. Akinwande, D. et al. Graphene and two-dimensional materials for silicon technology. *Nature* **573**, 507–518 (2019).
9. Das, S. et al. Transistors based on two-dimensional materials for future integrated circuits. *Nat. Electron.* **4**, 786–799 (2021).
10. Radisavljevic, B., Radenovic, A., Brivio, J., Giacometti, V. & Kis, A. Single-layer mos2 transistors. *Nat. Nanotechnol.* **6**, 147–150 (2011).
11. Hoque, M. A. et al. Ultranarrow semiconductor ws2 nanoribbon field-effect transistors. *Nano Lett.* **25**, 1750–1757 (2025).
12. Jiang, J., Xu, L., Qiu, C. & Peng, L.-M. Ballistic two-dimensional inse transistors. *Nature* **616**, 470–475 (2023).
13. Wan, Y. et al. Low-defect-density ws2 by hydroxide vapor phase deposition. *Nat. Commun.* **13**, 4149 (2022).
14. Das, M. et al. High-performance p-type field-effect transistors using substitutional doping and thickness control of two-dimensional materials. *Nat. Electron.* **8**, 24–35 (2025).
15. Wang, Y. et al. P-type electrical contacts for 2d transition-metal dichalcogenides. *Nature* **610**, 61–66 (2022).
16. Schram, T. et al. Ws2 transistors on 300 mm wafers with beol compatibility. In *2017 47th European Solid-State Device Research Conference (ESSDERC)*, 212–215 (IEEE, 2017).
17. Backman, J., Lee, Y. & Luisier, M. Phonon-limited transport in two-dimensional materials: A unified approach for ab initio mobility and current calculations. *Phys. Rev. Appl.* **21**, 054017 (2024).
18. Poncé, S., Li, W., Reichardt, S. & Giustino, F. First-principles calculations of charge carrier mobility and conductivity in bulk semiconductors and two-dimensional materials. *Rep. Prog. Phys.* **83**, 036501 (2020).
19. Kim, S. Y., Park, S. & Choi, W. Enhanced carrier mobility of multilayer mos2 thin-film transistors by al2o3 encapsulation. *Appl. Phys. Lett.* **109**, 152101 (2016).
20. Illarionov, Y. Y. et al. Insulators for 2d nanoelectronics: the gap to bridge. *Nat. Commun.* **11**, 3385 (2020).
21. Shao, P.-Z. et al. Enhancement of carrier mobility in mos2 field effect transistors by a sio2 protective layer. *Appl. Phys. Lett.* **108**, 203105 (2016).
22. Huang, C., Yan, Z., Hu, C., Xiong, X. & Wu, Y. Performance and stability improvement of cvd monolayer mos2 transistors through hfo2 dielectrics engineering. *Appl. Phys. Lett.* **123**, 073503 (2023).
23. Song, J.-G. et al. Effect of al2o3 deposition on performance of top-gated monolayer mos2-based field effect transistor. *ACS Appl. Mater. Interfaces* **8**, 28130–28135 (2016).
24. Sebastian, A., Pendurthi, R., Choudhury, T. H., Redwing, J. M. & Das, S. Benchmarking monolayer mos2 and ws2 field-effect transistors. *Nat. Commun.* **12**, 693 (2021).
25. Knobloch, T. et al. The performance limits of hexagonal boron nitride as an insulator for scaled cmos devices based on two-dimensional materials. *Nat. Electron.* **4**, 98–108 (2021).
26. Laturia, A., Van de Put, M. L. & Vandenberghe, W. G. Dielectric properties of hexagonal boron nitride and transition metal dichalcogenides: from monolayer to bulk. *npj 2D Mater. Appl.* **2**, 6 (2018).
27. Illarionov, Y. Y. et al. Reliability of scalable mos2 fets with 2 nm crystalline caf2 insulators. *2D Mater.* **6**, 045004 (2019).
28. Kc, S., Longo, R. C., Wallace, R. M. & Cho, K. Computational study of mos2/hfo2 defective interfaces for nanometer-scale electronics. *ACS Omega* **2**, 2827–2834 (2017).
29. Singh, A. K., Hennig, R. G., Davydov, A. V. & Tavazza, F. Al2o3 as a suitable substrate and a dielectric layer for n-layer mos2. *Appl. Phys. Lett.* **107**, 053106 (2015).
30. Van Troeye, B. et al. Impact of interface and surface oxide defects on ws2 electronic properties from first principles. *ACS Nano* **19**, 11664–11674 (2025).
31. Brandbyge, M., Mozos, J.-L., Ordejón, P., Taylor, J. & Stokbro, K. Density-functional method for nonequilibrium electron transport. *Phys. Rev. B* **65**, 165401 (2002).
32. Klinkert, C. et al. 2-d materials for ultrascaled field-effect transistors: One hundred candidates under the ab initio microscope. *ACS Nano* **14**, 8605–8615 (2020).

33. Afzalian, A., Akhoundi, E., Gaddemane, G., Duflou, R. & Houssa, M. Advanced dft–negf transport techniques for novel 2-d material and device exploration including hfs 2/wse 2 van der waals heterojunction tfet and wte 2/ws 2 metal/semiconductor contact. *IEEE Trans. Electron Devices* **68**, 5372–5379 (2021).
34. Lee, Y., Fiore, S. & Luisier, M. Ab initio mobility of single-layer mos 2 and ws 2: comparison to experiments and impact on the device characteristics. In *2019 IEEE International Electron Devices Meeting (IEDM)*, 24–4 (IEEE, 2019).
35. Datta, S. Nanoscale device modeling: the green's function method. *Superlattices Microstructures* **28**, 253–278 (2000).
36. Luisier, M., Schenk, A., Fichtner, W. & Klimeck, G. Atomistic simulation of nanowires in the sp 3 d 5 s* tight-binding formalism: From boundary conditions to strain calculations. *Phys. Rev. B-Condens. Matter Mater. Phys.* **74**, 205323 (2006).
37. Niquet, Y.-M. et al. Quantum calculations of the carrier mobility: Methodology, matthiessen's rule, and comparison with semi-classical approaches. *J. Appl. Phys.* **115**, 054512 (2014).
38. Luisier, M. Phonon-limited and effective low-field mobility in n-and p-type [100]-,[110]-, and [111]-oriented si nanowire transistors. *Appl. Phys. Lett.* **98**, 032111 (2011).
39. Ziogas, A. N. et al. A data-centric approach to extreme-scale ab initio dissipative quantum transport simulations. In *Proceedings of the International Conference for High Performance Computing, Networking, Storage and Analysis*, 1–13 (2019).
40. Gopalan, S., Van de Put, M. L., Gaddemane, G. & Fischetti, M. V. Theoretical study of electronic transport in two-dimensional transition metal dichalcogenides: Effects of the dielectric environment. *Phys. Rev. Appl.* **18**, 054062 (2022).
41. Lherbier, A. et al. Two-dimensional graphene with structural defects: elastic mean free path, minimum conductivity, and anderson transition. *Phys. Rev. Lett.* **106**, 046803 (2011).
42. Ducry, F. et al. Oxide induced degradation in mos2 field-effect transistors. *In preparation* (2025).
43. Draper, N. & Smith, H.*Applied regression analysis* (John Wiley & Sons, 1998).
44. Gong, Y., Carozo, V., Li, H., Terrones, M. & Jackson, T. N. High flex cycle testing of cvd monolayer ws2 tfts on thin flexible polyimide. *2D Mater.* **3**, 021008 (2016).
45. Jiang, J. et al. A facile and effective method for patching sulfur vacancies of ws2 via nitrogen plasma treatment. *Small* **15**, 1901791 (2019).
46. Fiore, S., Klinkert, C., Ducry, F., Backman, J. & Luisier, M. Influence of the hbn dielectric layers on the quantum transport properties of mos2 transistors. *Materials* **15**, 1062 (2022).
47. Lan, H.-Y., Tripathi, R., Appenzeller, J. & Chen, Z. Near-ideal subthreshold swing in scaled 2d transistors: The critical role of monolayer hbn passivation. *IEEE Electron Device Lett.* **45**, 1337–1340 (2024).
48. Zeng, D. et al. Single-crystalline metal-oxide dielectrics for top-gate 2d transistors. *Nature* **632**, 788–794 (2024).
49. International Roadmap for Devices and Systems (IRDS) 2023 Edition. https://irds.ieee.org/editions/2023 (2023). Accessed: 2024-12-10.
50. Ducry, F. et al. First principles modelling perspective for 2d channel–3d oxide interfaces. In *2024 8th IEEE Electron Devices Technology & Manufacturing Conference (EDTM)*, 1–3 (IEEE, 2024).
51. Kühne, T. D. et al. Cp2k: An electronic structure and molecular dynamics software package-quickstep: Efficient and accurate electronic structure calculations. *J. Chem. Phys.* **152**, 194103 (2020).
52. Perdew, J. P. et al. Restoring the density-gradient expansion for exchange in solids and surfaces. *Phys. Rev. Lett.* **100**, 136406 (2008).
53. Grimme, S., Antony, J., Ehrlich, S. & Krieg, H. A consistent and accurate ab initio parametrization of density functional dispersion correction (dft-d) for the 94 elements h-pu. *J. Chem. Phys.* **132**, 154104 (2010).
54. Grimme, S., Ehrlich, S. & Goerigk, L. Effect of the damping function in dispersion corrected density functional theory. *J. Computational Chem.* **32**, 1456–1465 (2011).
55. Goedecker, S., Teter, M. & Hutter, J. Separable dual-space gaussian pseudopotentials. *Phys. Rev. B* **54**, 1703 (1996).
56. Brück, S., Calderara, M., Bani-Hashemian, M. H., VandeVondele, J. & Luisier, M. Efficient algorithms for large-scale quantum transport calculations. *J. Chem. Phys.* **147**, 074116 (2017).
57. Stieger, C., Szabo, A., Bunjaku, T. & Luisier, M. Ab-initio quantum transport simulation of self-heating in single-layer 2-d materials. *J. Appl. Phys.* **122**, 045708 (2017).
58. Wang, M. A. & Pop, E. Monte carlo simulation of electrical transport with joule heating and strain in monolayer mos2 devices. *Nano Lett.* **25**, 6841–6847 (2025).
59. Datta, S., Assad, F. & Lundstrom, M. S. The silicon mosfet from a transmission viewpoint. *Superlattices Microstructures* **23**, 771–780 (1998).
60. Singh, R. & Ulrich, R. K. High and low dielectric constant materials. *Electrochem. Soc. Interface* **8**, 26 (1999).
61. Momma, K. & Izumi, F. Vesta 3 for three-dimensional visualization of crystal, volumetric and morphology data. *Appl. Crystallogr.* **44**, 1272–1276 (2011).

Acknowledgements

This research was supported by the NCCR MARVEL, funded by the Swiss National Science Foundation (SNSF) under Grant No. 205602, and by the Swiss National Supercomputing Center (CSCS) under projects s1119, s1212, and lp16. The authors acknowledge the Imec Industrial Affiliation Program (IIAP) for funding.

Author contributions

M.D., M.L., A.A., and G.P. conceived the project idea. M.D. run all DFT and quantum transport calculations. B.V.T. constructed the atomistic supercells. F.D. and J.C. provided guidance with simulations. All authors participated in the discussion of the results and contributed to the manuscript writing.

Competing interests

The authors declare no competing interests.

Additional information

Supplementary information The online version contains supplementary material available at https://doi.org/10.1038/s41699-025-00587-9.

Correspondence and requests for materials should be addressed to Mauro Dossena or Mathieu Luisier.